LA-UR-84-1235
CONF

Los Alamos National Laboratory is operated by the University of California for the United States Department of Energy under contract W-7405-ENG-36.

CONF-840415--20

LA-UR--84-1235

DE84 011354

TITLE: REACTIVE RESONANCE AND ANGULAR DISTRIBUTIONS IN THE ROTATING LINEAR MODEL

AUTHOR(S): Edward F. Hayes and Robert B. Walker

SUBMITTED TO: ACS Symposium Series, St. Louis, MO, April 9-12, 1984

DISCLAIMER

MASTER

Los Alamos Los Alamos National Laboratory
Los Alamos, New Mexico 87545

FORM NO 836 R4
ST NO 2629 5/81

REACTIVE RESONANCES AND ANGULAR DISTRIBUTIONS IN THE ROTATING LINEAR MODEL

Edward F. Hayes
National Science Foundation
Washington, DC 20550

and

Robert B. Walker
Group T-12, MSJ569
Los Alamos National Laboratory
Los Alamos, New Mexico 87545

In this paper, we will present a detailed analysis of the way in which resonances may affect the angular distribution of the products of reactive collisions. To do this, we have used an approximate three-dimensional (3D) quantum theory of reactive scattering (the Rotating Linear Model, or RLM) to generate the detailed scattering information (S-matrices) needed to compute the angular distribution of reaction products. We also employ a variety of tools, notably lifetime matrix analysis, to characterize the importance of a resonance mechanism to the dynamics of reactions. As a result, we hope to gain insight into how the resonant component of the scattering mechanism is manifested in the angular distribution of reaction products. Applications of these techniques to two reactive systems, $F+H_2$ and $He+H_2^+$, will be reviewed.

The Rotating Linear Model

The study of quantum effects such as resonances in atom-molecule reactions has been largely confined to coupled-channel calculations for collisions constrained to collinear geometries. Progress in quantum reactive scattering techniques is reviewed periodically (1-4). A few three dimensional (3D) quantum calculations of simple reactions, some more approximate (5-21) than others (22-23), have seen resonance features in reaction dynamics, and with the increasing sophistication and sensitivity of molecular beam experiments (24-27), it has become evident that the angular distribution of reaction products is likely to be the most sensitive observable manifestation of resonant contributions to reaction mechanisms.

Coupled channel methods for collinear quantum reactive calculations are sufficiently well developed that calculations can be performed routinely. Unfortunately, collinear calculations cannot provide any insight into the angular distribution of reaction products, because the impact parameter dependence of reaction probabilities is undefined. On the other hand, the best approximate 3D methods for atom-molecule reactions are computationally very intensive, and for this reason, it is impractical to use most 3D approximate methods to make a systematic study of the effects of potential surfaces on resonances, and therefore the effects of surfaces on reactive angular distributions. For this reason, we have become interested in an approximate model of reaction dynamics which was proposed many years ago both by Child (28), Connor and Child (29), and by Wyatt (30). This Rotating Linear Model (RLM) of reactions is in some sense a 3D theory of reactions, because the line upon which reaction occurs is allowed to tumble freely in space. A full three-dimensional theory would treat motion of the six coordinates (in the center of mass) associated with the two vectors $\vec{r}$ and $\vec{R}$ which specify the internuclear diatomic axis and the atom-molecule separation respectively. In a space-fixed frame, these vectors have polar coordinates (r,θ',ϕ') and (R,θ,ϕ). In the RLM, two degrees of freedom are eliminated by requiring the polar coordinates of the $\vec{r}$ and $\vec{R}$ vectors to coincide. The Hamiltonian for this system treats the four degrees of freedom associated with the coordinates (R,r,θ,ϕ). As a model for angular distributions for

reactive collision dynamics, the RLM possesses two attractive features. First, the angular degrees of freedom are handled in a partial wave expansion in the total angular momentum index ℓ, which introduces an impact parameter into the theory. Second, the RLM coupled-channel equations for each partial wave, when expressed in either Cartesian, polar, or hyperspherical coordinates, are identical to those of a purely collinear formulation, with the addition of an effective centrifugal potential

$$V^{\ell}_{RLM}(r,R) = h^2 \frac{[\ell(\ell+1)+1]}{2\mu(R^2+r^2)} \qquad (1)$$

to the collinear potential energy surface for reaction. Consequently, the solution of the reaction dynamics in the RLM is only as difficult in practice as solving a family of collinear problems, one for each partial wave. In enforcing asymptotic boundary conditions, we use spherical Bessel functions and ignore the centrifugal zero-point motion $1/(R^2+r^2)$ in Equation 1.

The obvious defect of the RLM is that it neglects motion of the $\vec{r}$ vector relative to the $\vec{R}$ vector. Asymptotically, the neglected degrees of freedom describe the rotational motion of the diatomic, and in the interaction region, describe the internal bending of the collision complex. Since the model only samples the collinear

projection of the entire potential hypersurface, one would expect RLM to be most reliable for those reactions which proceed through strongly hindered linear collision intermediates. In order to improve the quantitative aspects of the dynamics, especially in the reaction threshold region, we have added a bending correction to the RLM, in the same spirit as described earlier (31-34) for other models. The model thus generated is called the Bending Corrected Rotating Linear Model (BCRLM), and the results we describe here will all be derived from this model. The details of the bending correction are described in an earlier publication (35).

In a series of recent papers (35-38), we have used the BCRLM to examine the manifestation of resonances for several reactions, including

$$F+H_2(v) \rightarrow HF(v') + H$$

$$H+H_2(v) \rightarrow H_2(v') + H$$

and several of their isotopic variants. In these papers, we have considered the importance of quantum effects, especially resonances, upon integral and differential cross sections and upon rate constants for these reactions. The hope is that these approximate results contain many of the important features of the more accurate theoretical methods. At any total scattering energy E, elements of

the multichannel S-matrix in the RLM are labelled by the total angular momentum index ℓ, and by the initial and final vibrational quantum numbers v and v'. Equations for physical observables in the RLM have been given previously (28-30), and we only summarize the final results here, in order to establish a common notation. The opacity function gives the impact parameter dependence of the reaction probabilities at fixed E, so that

$$P^{\ell}_{vv'}(E) = \left|S^{\ell}_{vv'}(E)\right|^2 \quad , \tag{2}$$

where the impact parameter is related to the angular momentum index by the semiclassical expression $bk \simeq (\ell+1/2)$, and k is the translational wavenumber. The angular distribution of products of reaction $I_{vv'}(\theta)$ is the differential cross section

$$d\sigma_{vv'}(\theta,\phi;E)/d\Omega = \left|f_{vv}(\theta,\phi;E)\right|^2 \equiv I_{vv'}(\theta) \tag{3}$$

where the scattering amplitude is

$$f_{vv'}(\theta,\phi;E) = (2ik_v)^{-1} \sum_{\ell} (2\ell+1)(\delta_{vv'}-S^{\ell}_{vv}(E))P_{\ell}(\cos\theta) \tag{4}$$

The integrated cross section is

$$\sigma_{vv'}(F) = 2\pi \int I(\theta)\sin\theta d\theta = \pi k^{-2} \sum_{\ell} (2\ell+1)P^{\ell}_{vv'}(E) \tag{5}$$

All angular distributions reported in this paper are calculated using Equations (3) and (4) above. However, in interpreting features of the angular distribution, it is often instructive to appeal to the elements of the classical formula for angular distributions

$$I_{vv'}(\theta) = \frac{b\, P_{vv'}(b)}{\sin\theta \left|\frac{d\theta(b)}{db}\right|} \qquad (6)$$

In Equation (6), $\theta(b)$ is the classical deflection function, and specifies the angle θ at which the particles separate after a collision at an initial impact parameter b. The deflection function has the quantum analog

$$\theta_q(\ell) \equiv \frac{d\, \mathrm{Arg}(S^{\ell}_{vv'}(E))}{d\ell} \qquad (7)$$

where Arg(z) is the phase angle of the complex number z. Equation (3), (4), (6) and (7) make it clear that the shape of the angular distribution of reaction products depends both on the magnitudes and phases of the elements of the S-matrix.

Analysis of Resonances

Resonances modify what would have otherwise been the energy and impact parameter dependence of the phases and magnitudes of the S-matrix elements. Resonances therefore alter the shape of the angular distribution function. Kuppermann (39) has recently reviewed many of the tools which can be used to characterize resonances in single and multichannel problems. The analysis of resonances in a multichannel problem is simplest if one assumes (41-46) the isolated narrow resonance conditions (INR), in which a resonance is due to a single simple pole of the S-matrix located at energy $E = E_R - i\Gamma/2$ in the complex plane. It is assumed that the

background or direct component of the scattering has a much slower energy dependence than the resonant component, which is equivalent to requiring that the resonance width Γ be small, and that the pole lie close to the real axis. The slowly varying background contribution condition will be compromised if there is either a new channel threshold near the resonance energy E_R, or if there are other nearby (overlapping) resonances.

The effect of resonances on angular distributions in reactive scattering can be effectively modeled if one can successfully separate the multichannel S-matrix into its background and resonant components, so that

$$S = S_0 + S_R \quad , \tag{8}$$

where it will be understood in what follows that this analysis is done at each partial wave index ℓ. Invoking the INR conditions, Equation 8 can be written in a generalization of the single-channel Breit-Wigner form

$$S = S_0^{1/2}\left(1 - \frac{i\gamma\gamma^T}{E - z}\right) S_0^{1/2} \tag{9}$$

with $z=E_R-i\Gamma/2$. For N open channels, column vector $\underline{\gamma}$ is composed of N real numbers, such that $\gamma^T\gamma=\Gamma$. Comparing Equations (8) and (9) makes it clear that the complete characterization of the resonant and background parts of the S-matrix requires knowledge of the resonant partial widths ($S_0^{1/2}\gamma$), where

$$S_R = \frac{-i(S_0^{1/2}\gamma)(S_0^{1/2}\gamma)^T}{E - z} \tag{10}$$

All resonances are necessarily characterized by the lifetime of the compound state, and Smith's (47) definition of the lifetime matrix is

$$Q = i\hbar S \frac{dS^{\dagger}}{dE} \tag{11}$$

If we substitute Equation (7) into Equation (11), we obtain a direct expression for Q in the vicinity of the resonance

$$Q = \frac{\hbar(S_0^{1/2}\gamma)(S_0^{1/2}\gamma)^{\dagger}}{(E-E_R)^2 + \Gamma^2/4} \tag{12}$$

In deriving Equation (12), we have assumed S_0 to be independent of E. It is also convenient to express Q as

$$Q = \frac{\hbar\Gamma}{(E-E_R)^2 + \Gamma^2/4}\ \omega\omega^{\dagger} \tag{13}$$

where the unit vector ω is

$$\omega = \Gamma^{-1/2} S_0^{1/2}\gamma \tag{14}$$

Equation (13) tells us two things about the lifetime matrix near an INR: (1) the trace of $\underline{Q}$ has the expected single-channel Lorentzian form

$$\text{Trace } (Q) = \frac{\hbar\Gamma}{(E-E_R)^2 + \Gamma^2/4} \tag{15}$$

and (2) that all the eigenvalues of Q are zero except for one (Q is a rank 1 matrix). Furthermore, the eigenvector of Q corresponding

ideally to the nonzero eigenvalue is the unit vector ω defined in Equation (14). Combining Equation (14) and (10) gives a direct expression for S_R in terms of the appropriate eigenvector of Q, namely

$$S_R = \frac{i\Gamma\omega\omega^T}{E-E_R + i\Gamma/2} \tag{16}$$

Combining Equation (16) with Equation (8) allows a determination of the background S-matrix S_0, and from S_0 at each partial wave one can calculate the angular distribution in the absence of a resonance, Equation (3). In practice, the breakdown of the INR conditions, especially the energy dependence of S_0, compromises the practical application of the preceding discussion, but as we hope to show, the scheme outlined nevertheless seems quite useful in analyzing resonances.

Resonance Effects On Quantum Deflection Functions

In a recent paper (37) we explored the effects of resonances on the phase behavior of individual elements of the S-matrix, with particular attention paid to the quantum deflection function, defined in Equation (7). Following in the spirit of Child's (43) analysis, we assume the partial wave dependence of the resonance energy to be

$$E_R(\ell) = E_R(0) + B\ell(\ell+1) \tag{17}$$

and further assume the resonance width has a quadratic dependence on ℓ

$$\Gamma_\ell = \Gamma_0(1+a\ell+b\ell^2) \tag{18}$$

If we then assume that the phase behavior of a single off-diagonal element of the S-matrix is

$$S^\ell_{vv'} = |S^\ell_{vv'}| e^{i\delta^\ell_{vv'}} , \tag{19}$$

$$\delta^\ell_{vv'} = \delta^\ell_{vv'}(\text{background}) + \delta^\ell_{vv'}(\text{resonant}) , \tag{20}$$

$$\tan \delta^\ell_{vv'}(\text{resonant}) = \frac{\Gamma_\ell/2}{E_R(\ell)-E} , \tag{21}$$

then Equations (17-21) lead to the following expression for the behavior of the quantum deflection function near a resonance,

$$\Theta_{vv'}(\ell) = \Theta^0_{vv'}(\ell) + \frac{1}{2} \frac{\Gamma_0(a+2b\ell)(E_R-E) - B\Gamma_\ell(2\ell+1)}{(E_R(\ell)-E)^2 + \Gamma^2_\ell/4} \tag{22}$$

Note in Equations (19)-(22) that there is a factor of two difference assumed in the dependence of the off-diagonal resonant phase behavior from that of single channel behavior. This assumption follows from Equation (9). In an earlier paper (37), we showed that Equation (22) (with a=b=0) was remarkably good in modeling the resonant behavior of the deflection function.

Application to Angular Distributions

In this section, we present an application of the techniques described in the previous sections to the angular distribution for the reaction

$F+H_2(v'=0) \rightarrow HF(v'=2)+H$

A series of calculations, using the BCRLM, was performed on the M5 surface (48), as reported earlier (37). Here we will concentrate on the angular distribution at a fixed total energy E=1.807 eV (measured from the minimum of the HF vibrational potential for asymptotic H+HF geometries). The initial relative kinetic energy of reactants at this total energy is 0.162 eV (or 3.73Kcal/mol). We show the impact parameter dependence of the magnitudes and phases of the appropriate elements of the S-matrix in Figures (1) and (2). Figure (1) shows the opacity function, $P_{02}(\ell)$ vs. ℓ (see Equation (1)), and Figure (2) shows the quantum deflection function $\Theta_{02}(\ell)$ vs. ℓ (see Equation (7)). The presence of a resonant contribution to the reaction mechanism is evident as a dip in the deflection function over the range of ℓ values 12-20. The resonance is also manifested in the opacity function of Figure (1) as a significant enhancement (see later) of the reaction probability over the same range of ℓ values. The angular distribution which results from these S-matrix elements is shown in Figure 3.

Let us now analyze the resonance contribution to this angular distribution more closely. From Figure 2 it is evident that at E=1.807°eV, the resonant contribution to the deflection of products is greatest near ℓ=16. We therefore show in Figure 4 a plot of the eigenvalues of the ℓ=16 lifetime matrix (Equation (11)) as a function of totalenergy E. Over this range of total energies, there are are five open channels in the S-matrix (v=0 of reactants and v'=0,1,2,3 of products). It is clear in Figure 4 that a Lorentzian shaped feature is indeed centered near E=1.807 eV in one of the

eigenlifetime channels. If this feature is fitted to the form of Equation (17), with a quadratic background behavior, the resonance energy $E_R(16)$ and width Γ_{16} can be determined. Values of $E_R(\ell)$ and Γ_ℓ for other ℓ values are determined similarly. In Figure 5, we show a plot of the energy dependence of the magnitudes of the elements of the eigenvector of Q corresponding to the eigenvalues with the Lorentzian profile. These are related to the partial widths by Equation (14). Figures 4 and 5 give an indication of the degree of validity of the INR conditions for this problem. Although one of the eigenlifetime channels shows the resonance feature much more strongly than the others, the other eigenvalues are neither zero over the width of the resonance, nor are they even constant. Similarly, in Fig. 5, we see that the resonant partial widths are not necessarily slowly varying with energy over the width of the resonance.

Using the data of Figure 5 to generate the partial widths, we calculate the resonant part of the S-matrix using Equation (16), and the background S-matrix using Equation (8). Because the elements of the ω vector in Equation (16) come from the diagonalization of Q calculated using Equation (11), we obtain ω with an arbitrary phase $e^{-i\Theta}$. Possible choices of Θ are determined by requiring the background S-matrix S_0 be unitary (in addition to being symmetric). At energies $E=E_R(\ell)$, only one value of Θ makes S_0 unitary, and at other values of E, there are two values of E which suffice. The physically satisfactory root is the one for which the resonant behavior of S_0 is eliminated (the other root tends to accentuate the resonance). An example of this procedure is demonstrated in Figure 6, where we have plotted $|S^{16}_{02}(E)|$ vs. E.

The solid line shows the magnitudes of the full S-matrix elements, the solid circles show the background S-matrix elements corresponding to the physical root, and the open circles show background S-matrix elements corresponding to the nonphysical root.

Assembling the magnitudes of the background S-matrix elements for the physical roots at all partial waves from ℓ=0 to 18, we construct the background opacity function shown as the solid curve in Figure 7, at E = 1.807 eV. The large dip in this opacity function near ℓ=12 is the result of the crossing of two eigenvalues of the lifetime matrix in this range of ℓ and E. The crossing eigenvalues induce interactions between the eigenvectors and perturb the calculation of the background S-matrix. Consequently, we have also used the opacity function given by the dashed line in Figure 7 to produce an estimate of the background angular distribution. Furthermore, because of the practical difficulties with the determination of the magnitudes of the background S-matrix elements, we elected not to use the phases determined in this manner, but to use phases from the deflection function analysis described earlier. The set of resonance energies is reasonably described by the form of Equation (18) with $E_R(0)$ = 1.7234 eV and B = 3.05×10^{-4} eV, and the ℓ-dependence of the widths is adequately described by Equation (18) with Γ_0 = 0.031 eV, and a=b=3.11×10^{-3}. We then use Equation (22) to produce the background deflection function $\Theta^0_{vv'}(\ell)$, and we show results in Figure 8 as the solid curve. The dashed curve is the full deflection function of Figure 2, shown for comparison. Phases of the background S-matrix elements are determined, up to an unimportant constant, by integrating $\Theta^0_{vv'}(\ell)$. Having determined a

set of background S-matrix elements, we calculate an angular distribution due to the background scattering, shown in Figure 9 as the solid curve. The dashed curve shows the angular distribution of using the smoothed opacity function of Figure 7, and the dotted curve reproduces the distribution of Figure 3 for comparison.

The effect of the resonance contribution to the angular distribution in Figure 9 is twofold. The resonance (1) enhances the intensity of the sideways peak, and (2) the position of the sideways peak is shifted toward the forward direction by approximately 20°, an additional deflection which quantitatively agrees with the size of the dip in the deflection function shown in Figure 8. There is also a small reduction in the interference oscillations in the forward direction. It is significant to note, however, that the background angular distribution is sideways peaked, as a consequence of the generally increasing tendency of the opacity functions of Figure 7 at l[redacted] ℓ.

Forward Peaked Angular Distributions

In the remainder of this paper, we wish to consider the conditions which may lead to broad, or even forward-peaked, angular distributions of products at the reaction threshold. Such angular distributions have been observed in recent $F+H_2$ beam experiments (27), and within the context of the BCRLM, we have observed this phenomenon in several systems.

$F+H_2$. We see this sort of behavior in the reaction $F+H_2(v=0) \rightarrow HF(v'=2)+H$ on a modification of the M5 potential surface due to Truhlar, Garrett, and Blais (49). This modified surface differs

from the M5 surface in the following three qualitative ways: (1) the new surface has a lower collinear barrier to reaction, (2) has a softer bending potential in the entrance valley, and (3) has a much lower adiabatic barrier in the exit valley for reaction into the HF(v'=3) final state.

We show in Figures 10 and 11 a plot of the reactive probabilities for this system, for reactions into HF(v'=2) and HF(v'=3) respectively. While the qualitative shape of the probability curves for reaction to HF(v'=3) resembles that of the M5 potential surface, there is an obvious difference in the dynamics leading to HF(v'=2) products. At low partial waves, the reaction into HF(v'=2) is suppressed relative to the M5 case, and at larger partial waves, there is an obvious onset of resonance dynamics. Presumably, the exit valley adiabatic barrier which is present in the M5 surface, but has been removed in this newer surface, is replaced by a similar (but centrifugal) barrier at intermediate partial waves, thereby restoring the resonance mechanism. The effect on angular distributions is obvious. Figure 12 shows opacity function plots at several energies, and Figure 13 shows the corresponding angular distribution plots. The resonant mechanism in this case is considerably stronger than for the corresponding M5 calculation, and the effect on the angular distributions is to induce much stronger interference oscillations, since there are many fewer partial waves contributing significantly to the reaction. In the case of the reaction to produce HF(v'=3) on this surface, it is evident that the v'=3 state of products participates more strongly

in the resonance mechanism, as can be seen in the angular distribution plots of Figure 14. The angular distribution shifts from backward to sideways peaked, and has noticeable interference oscillations at all energies.

The $F+H_2$ reaction on this newer potential surface demonstrates one way in which the BCRLM will produce an angular distribution at the reaction threshold which is not smooth and backward-peaked. In this case, the absence of a significant reaction probability for low partial waves, and the appearance of a resonance feature at larger partial waves, combine to produce an opacity function which peaks at large partial waves, and hence an angular distribution which has a predominant forward distribution of reaction products. We have seen results similar to these in the angular distribution for the reactions $F+D_2(v=0) \rightarrow DF(v'=3,4)+D$ on this same surface.

$\underline{HeH_2^+}$. We performed a set of BCRLM calculations for the reaction $He+H_2^+ \rightarrow HeH^+ +H$ using the DIM representation (50) of the potential surface. A great many resonance features have been seen (51) in the collinear reactive dynamics of this system, and many have been identified with the attractive well which is present on this surface in the entrance valley. Because the bending potential predicted by the DIM surface is very weak, the BCRLM dynamics (for the $\ell=0$ partial wave) resembles that of the collinear calculation. Reaction probabilities for the reaction $He+H_2^+(v=3) \rightarrow HeH^+(v'=0)+H$ are shown in Figure 15 for several partial waves. The predominance of many resonances in each partial wave is evident in the figure. As written, this reaction is endothermic by 0.81 eV, but once the

endothermicity is provided by the kinetic energy of reactants, there is no barrier to the reactive process. Consequently, reaction occurs from many partial waves at the reaction threshold. There is little or no evidence of a centrifugal barrier to reaction appearing in the dynamics until the ℓ=15 partial wave. For this reason the opacity function, at the reaction threshold, contains contributions from a large number of partial waves, as can be seen in Figure 16. The resulting angular distributions of products are therefore quite broad, and show the effects of the multitude of resonances through the very oscillatory nature of the distributions, as is shown in Figure 16. Results similar to these, except for reaction from other initial vibrational states of the H_2^+ reactant molecule, are qualitatively the same -- reaction from many partial waves at threshold makes possible a very broad angular distribution of products.

Summary

We have attempted to describe here the way in which resonances in reactive scattering may affect the angular distribution of the products of reaction. To do this, we have employed a simple 3$\hat{D}$ model of reactions, the Bend-Corrected Rotating Linear Model, and have computed angular distributions for several reactive systems in which resonances contribute to the scattering dynamics.

The most straightforward way to determine the effect of resonances on angular distributions is to define a partition of the angular distribution into its direct and resonant components. We

described an attempt to do this for the reaction $F+H_2(v=0) \rightarrow HF(v'=2)+H$ at an energy where the angular distribution was decidedly sideways peaked. In this analysis, we found the effect of the resonant part of the scattering was to enhance the amplitude of the sideways peak, and to shift the peak to a more forward angle. The background angular distribution is still sideways peaked, however, lending further support to the conclusion which we (36-37) and others (52) have made earlier, that the presence of a sideways peak in the angular distribution is not necessarily the signature of a resonant process.

We have also sought to describe the conditions under which the angular distribution of reaction products could be forward-peaked at the reaction threshold, within the context of the BCRLM. Two sources of this effect have been seen in our calculations, and the essential feature which they have in common is that the reaction must, at threshold, contain contributions from scattering at large partial waves. In the example shown for the $F+H_2$ reaction on a modification (49) of this M5 surface, a forward peaked distribution at threshold was seen to result from a resonant mechanism which is absent in low partial waves, and becomes significant for larger partial waves. In the second example, for the $He+H_2^+$ reaction, forward peaked angular distributions at threshold result from the fact that the reaction proceeds without a barrier (other than that resulting from the overall endothermicity of reaction). In the $He+H_2^+$ reaction, there are indeed many resonances which contribute to the dynamics, but it is not clear that the angular distribution would not be peaked in the forward direction even in the absence of the resonances.

Literature Cited

1. Walker, R. B.; Light, J. C. Ann. Rev. Phys. Chem. 1980, 31, 401.
2. Schatz, G. C. In "Potential Energy Surfaces and Dynamics Calculation"; Truhlar, D. G., Ed.; Plenum: New York, 1981; Chap. 12.
3. Kuppermann, A. In "Theoretical Chemistry: Advances and Perspectives, Vol. 6A"; Academic: New York, 1981; p. 79-164.
4. Baer, M. Adv. Chem. Phys. 1982, 49, 191.
5. Wyatt, R. E. in "Horizons in Quantum Chemistry"; Fukui, K.; Pullman, B., eds.; Reidel: Dordrecht, 1980; p.
6. Redmon, M. J.; Wyatt, R. E. Chem. Phys. Letters 1979, 63, 209.
7. Wyatt, R. E.; McNutt, J. F; Redmon, M. J. Ber. Bunsenges. Phys. Chem. 1982, 86, 437.
8. Wyatt, R. E.; Redmon, M. J. Chem. Phys. Letters 1983, 96, 284.
9. Bowman, J. M.; Lee, K. T. Chem. Phys. Letters 1979, 64, 291.
10. Khare, V.; Kouri, D. J.; Baer, M. J. Chem. Phys. 1979, 71, 1188.
11. Bowman, J. M.; Lee, K. T. J. Chem. Phys. 1980, 72, 5071.
12. Jellinek, J.; Baer, M. J. Chem. Phys. 1982, 76, 4883.
13. Jellinek, J.; Baer, M. J. Chem. Phys. 1983, 78, 4494.
14. Jellinek, J.; Baer, M. Chem. Phys. Letters 1981, 82, 162.

15. Baer, M.; Khare, V.; Kouri, D. J. Chem. Phys. Letters 1979, 68, 378.

16. Baer, M.; Mayne, H. R.; Khare, V.; Kouri, D. J. Chem. Phys. Letters 1980, 72, 269.

17. Kouri, D. J.; Khare, V.; Baer M. J. Chem. Phys. 1981, 75, 1179.

18. Jellinek, J.; Baer, M.; Khare, V.; Kouri, D. J. Chem. Phys. Letters 1980, 75, 460.

19. Baer, M.; Jellinek, J.; Kouri, D. J. Chem. Phys. 1983, 78, 2962.

20. Shoemaker, C. L.; Kouri, D. J.; Jellinek, J.; Baer, M. Chem. Phys. Letters 1983, 94, 359.

21. Schatz, G. C. Chem. Phys. Letters 1983, 94, 183.

22. Schatz, G. C.; Kuppermann, A. Phys. Rev. Letters 1975, 35, 1266.

23. Walker, R. B.; Stechel, E. B.; Light, J. C. J. Chem. Phys. 1978, 69, 2922.

24. Sparks, R. K.; Hayden, C. C.; Shobatake, K.; Neumark, D. M.; Lee, Y. T. in "Horizons in Quantum Chemistry"; Fukui, K.; Pullman, B., Eds.; Reidel: Dordrecht, 1980, p.

25. Lee, Y. T. Ber. Bunsenges. Phys. Chem. 1982, 86, 378.

26. Hayden, C. C. PhD. Thesis, Lawrence Berkeley Laboratory, LBL-13660, Berkeley, California, 1982.

27. Neumark, D. M.; Wodtke, A. M.; Robinson, G. N.; Lee, Y. T. see the contribution in this volume.

28. Child, M. S. Mol. Phys. 1967, 12, 401.

29. Connor, J.N.L.; Child, M. S. Mol. Phys. 1970, 18, 653.

30. Wyatt, R. E. J. Chem. Phys. 1969, 51, 3489.

31. Mortensen, E. M. J. Chem. Phys. 1968, 48, 4029.

32. Mortensen, E. M.; Pitzer, K. S. Chem. Soc. Spec. Publ. 1962, 16, 57.

33. Garrett, B. C.; Truhlar, D. G. J. Am. Chem. Soc. 1979, 101, 4534.

34. Bowman, J. M.; Ju, G.-Z.; Lee, K. T. J. Phys. Chem. 1982, 86, 2232.

35. Walker, R. B.; Hayes, E. F. J. Phys. Chem. 1983, 87, 1255.

36. Walker, R. B.; Hayes, E. F. J. Phys. Chem. 1984, to be published.

37. Hayes, E. F.; Walker, R. B. J. Phys. Chem., accepted.

38. Walker, R. B.; Blais, N. C.; Truhlar, D. G. J. Chem. Phys. 1983, 80, 246.

39. Kuppermann, A. In "Potential Energy Surfaces and Dynamics Calculations"; Truhlar, D. G., Ed.; Plenum: New York, 1981; Chap. 16.

40. Kaye, J.; Kuppermann, A. J. Phys. Chem. 1981, 85, 1969.

41. Taylor, J. R. "Scattering Theory"; Wiley: New York, 1972; p. 407-417.

42. Wu, T.-Y.; Ohmura, T. "Quantum Theory of Scattering"; Prentice-Hall: Englewood Cliffs, N.J., 1962; pp. 20-22, 427-429.

43. Child, M. S. "Molecular Collision Theory"; Academic: New York, 1974; pp. 53-56, 73-75.

44. Ashton, C. J.; Child, M. S.; Hutson, J. M. J. Chem. Phys. 1983, 78, 4025.

45. Skodje, R. T.; Schwenke, D. W.; Truhlar, D. G.; Garrett, B. C. J. Phys. Chem. 1984, 88, 628.

46. Skodje, R. T.; Schwenke, D. W.; Truhlar, D. G.; Garrett, B. C. J. Chem. Phys. 1984, to be published.

47. Smith, F. T. Phys. Rev. 1960, 118, 349.

48. Muckerman, J. T. In "Theoretical Chemistry: Advances and Perspectives, Vol. 6A"; Academic: New York, 1981; p. 1.

49. Truhlar, D. G.; Garrett, B. C.; Blais, N. C. J. Chem. Phys. 1984, 80, 232. The modified surface used in the current paper is a slight modification of the Sato parameter for new surface number two in this reference. The value for the Sato parameter for new surface number two is 0.106. The current value, which removes the adiabatic barrier in the exit valley for the $F+D_2$ isotopic combination, is 0.168.

50. Kuntz, P. J. Chem. Phys. Letters 1972, 16, 581.

51. Adams, J. T. Chem. Phys. Letters 1975, 33, 275.

52. Agmon, N. Chem. Phys. 1981, 61, 189.

FIGURE CAPTIONS

Figure 1. Opacity function, $P(\ell)$ vs. ℓ, for the reaction $F+H_2(v=0) \rightarrow HF(v'=2)+H$ at total energy E = 1.807 eV. The peak near $\ell=14$ is characteristic of a resonance contribution to the overall reaction dynamics.

Figure 2. Quantum deflection function, $\Theta(\ell)$, as defined by Equation 7, for the reaction $F+H_2(v=0) \rightarrow HF(v'=2)+H$ at total energy E = 1.807 eV. The dip near $\ell=16$ a manifestation of the resonance mechanism, because the longer-lived collision complex rotates more toward forward angles.

Figure 3. Angular distribution, or differential scattering cross section for the BCRLM reaction $F+H_2(v=0) \rightarrow HF(v'=2)+H$ at total energy E = 1.807 eV.

Figure 4. Eigenvalues of the collision lifetime matrix Q (see Equation 11) for the $\ell=16$ partial wave of the $F+H_2$ reaction. The resonance near total energy E = 1.8 eV is evident in one of the eigenvalues.

Figure 5. Energy dependence of the magnitudes of the elements of the eigenvector of Q corresponding to the resonant eigenvalue. Near the resonant energy E = 1.806 eV, the channels which participate most in the resonance dynamics are clearly v=0 of the H_2 reactants and v'=2 of the HF products.

Figure 6. Magnitudes of background S-matrix elements for the reaction $F+H_2(v=0) \rightarrow HF(v'=2)+H$, partial wave $\ell=16$. The solid curve shows the full S-matrix elements, and the open and filled circles show two choices of background elements corresponding to the two phase choices for the partial widths (see text). The open circles are elements corresponding to a nonphysical root, the closed circles correspond to the physical root.

Figure 7. Background opacity function for the reaction $F+H_2(v=0) \rightarrow HF(v'=2)+H$ at E = 1.807 eV. The solid curve is the direct result of the extraction procedure discussed in the text, and the dashed curve is a smoothed version.

Figure 8. Background deflection function for the reaction $F+H_2 \rightarrow HF(v'=2)+H$ at E = 1.807 eV. The solid curve removes the resonance contribution using Equation (23). The dashed curve reproduces the full deflection function of Figure 2 for comparison.

Figure 9. Background angular distributions for the reaction $F+H_2(v=0) \rightarrow HF(v'=2)+H$ at E = 1.807 eV. The solid curve used the opacity function shown in Figure 7 as a solid curve, and the smoother, dashed curve shows the angular distribution which results from the smoothed opacity function of Figure 7. The dotted curve reproduces the full angular distribution of Figure 3 for comparison.

Figure 10, Reaction probabilities vs. energy for the reaction $F+H_2(v=0) \rightarrow HF(v'=2)+H$ on a recent modification (49) of the M5 surface. Curves are shown for partial waves $\ell=0,5,10,\ldots30$. Note the resonance feature which builds in at large partial waves.

Figure 11. Reaction probabilities vs. energy for the reaction $F+H_2(v=0) \rightarrow HF(v'=3)+H$ on a recent modification (49) of the M5 surface. Curves are shown for $\ell=0,5,10,\ldots30$. Note the reduced delay in the threshold for reaction at low partial waves.

Figure 12. Opacity functions for the reaction $F+H_2(v=0) \rightarrow HF(v'=2)+H$ on a recent modification (49) of the M5 surface. curves are shown at several scattering energies. Note that almost all the scattering at each energy arises from only a few, large ℓ partial waves.

Figure 13. Angular distributions for the reaction $F+H_2(v=0) \rightarrow HF(v'=2)+H$ on a recent modification (49) of the M5 surface. Curves are shown at the same energies as Figure 12.

Figure 14. As in Figure 13, angular distribution for the reaction $F+H_2(v=0) \rightarrow HF(v'=3)+H$ on a recent modification of the M5 surface. The interference oscillations indicate that the HF(v'=3) channel participates in the resonance dynamics for this surface.

Figure 15. Reaction probabilities vs. energy for the reaction He + $H_2^+(v=3)$ + $HeH^+(v'=0)$+H on the DIM surface of reference (50). Curves are shown for ℓ=0,5,10,...,30.

Figure 16. Angular distributions for the reaction He + $H_2^+(v=3)$ + $HeH^+(v'=0)$+H. Curves are shown at total energies (measured from the minimum of the H_2^+ entrance valley well) E = 1.0, 1.1, 1.2, and 1.3 eV.

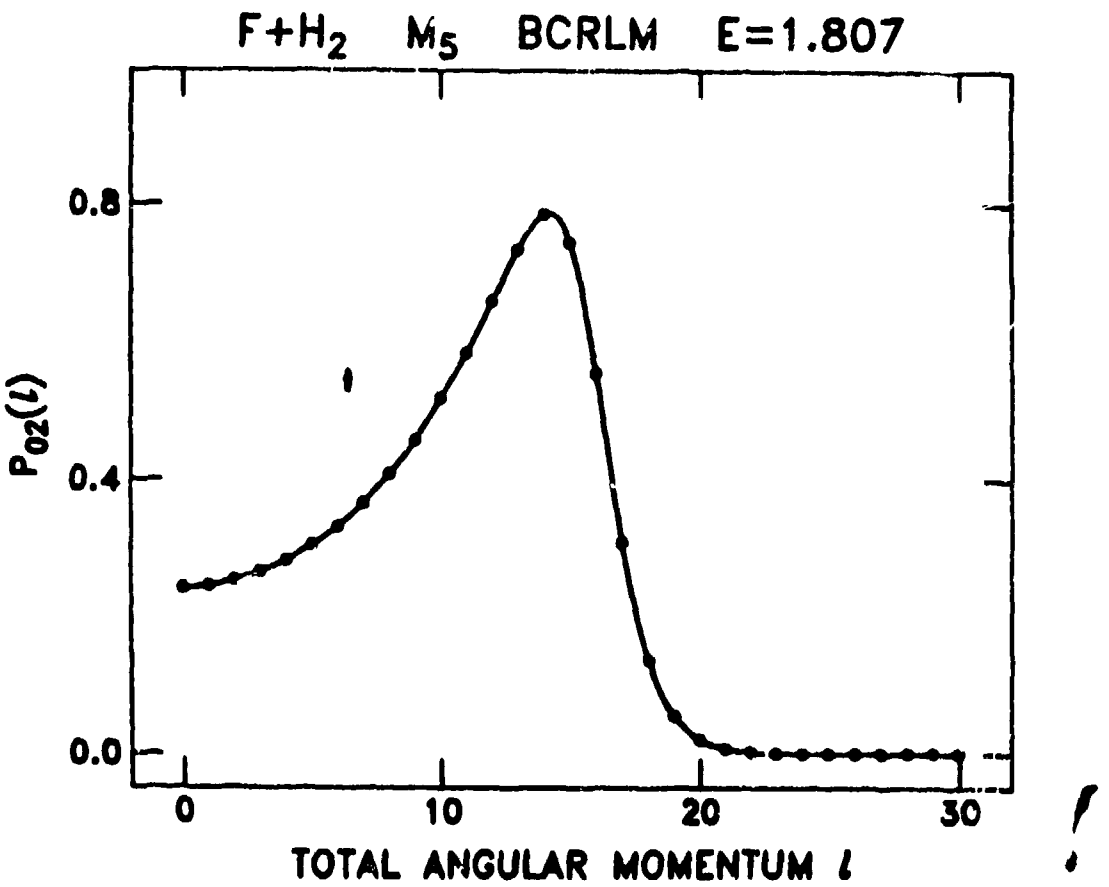

Figure 1. Opacity function, $P(\ell)$ vs. ℓ, for the reaction $F+H_2(v=0) \rightarrow HF(v'=2)+H$ at total energy $E = 1.807$ eV. The peak near $\ell=14$ is characteristic of a resonance contribution to the overall reaction dynamics.

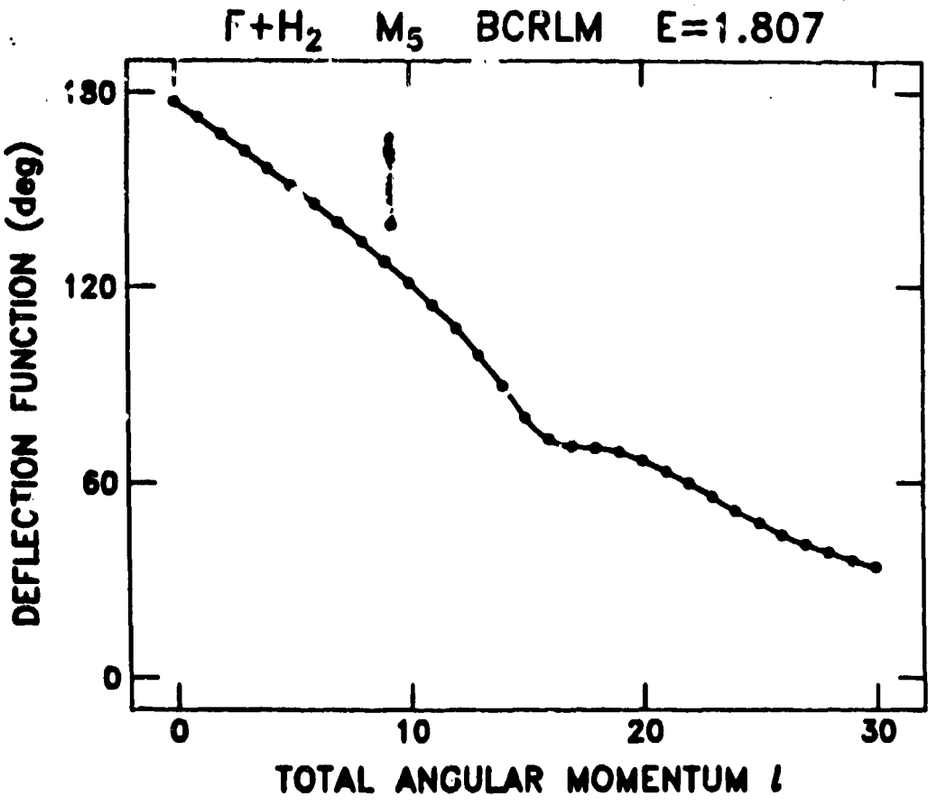

Figure 2. Quantum deflection function, $\Theta(L)$, as defined by Equation 7, for the reaction $F+H_2(v=0) \rightarrow HF(v'=2)+H$ at total energy $E = 1.807$ eV. The dip near $L=16$ a manifestation of the resonance mechanism, because the longer-lived collision complex rotates more toward forward angles.

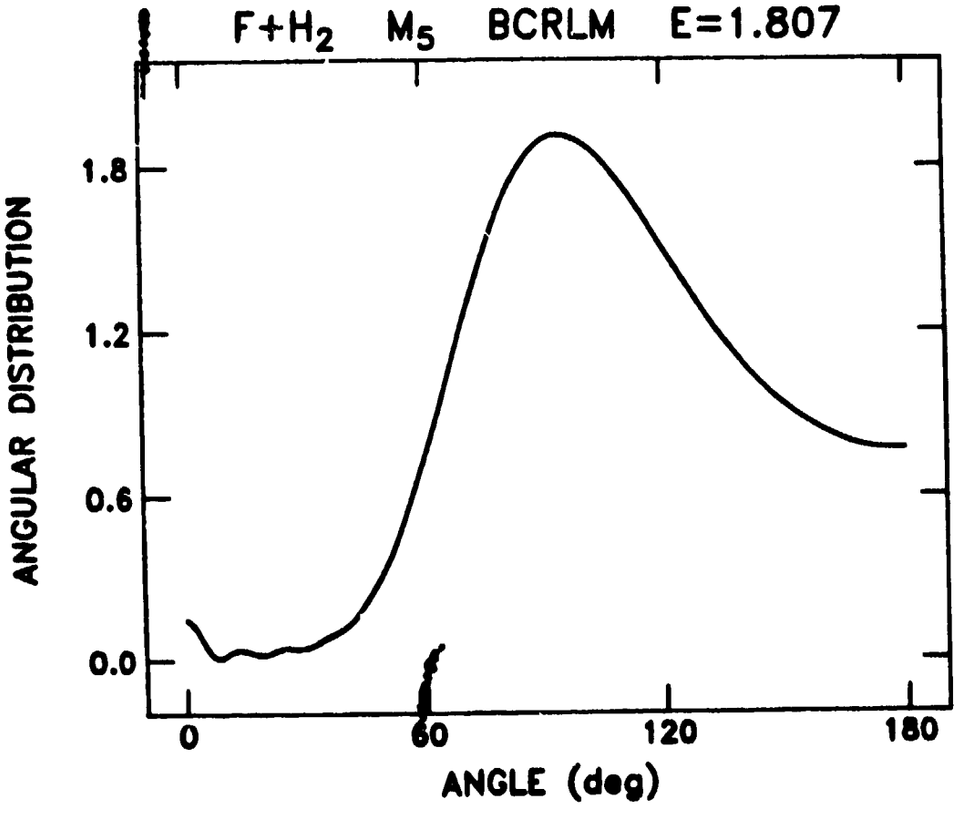

Figure 3. Angular distribution, or differential scattering cross section for the BCRLM reaction $F+H_2(v=0) \rightarrow HF(v'=2)+H$ at total energy $E = 1.807$ eV.

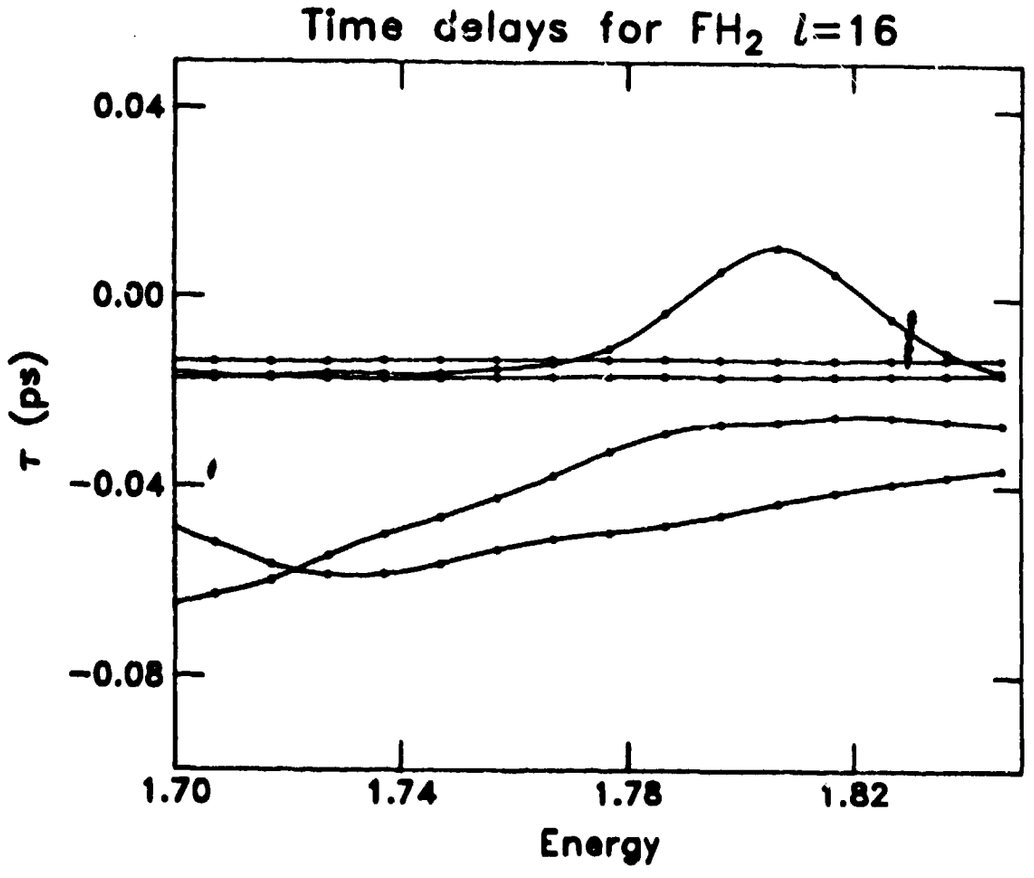

Figure 4. Eigenvalues of the collision lifetime matrix Q (see Equation 11) for the l=16 partial wave of the F+H_2 reaction. The resonance near total energy E = 1.8 eV is evident in one of the eigenvalues.

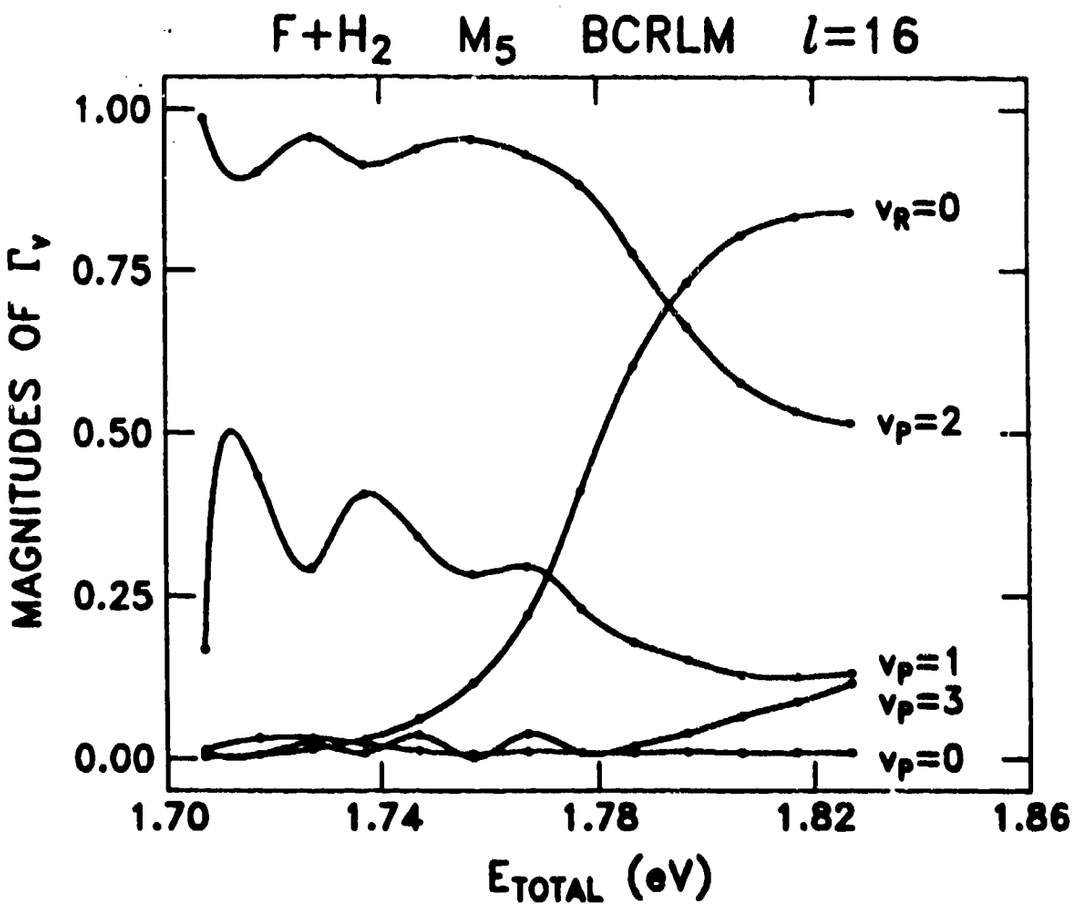

Figure 5. Energy dependence of the magnitudes of the elements of the eigenvector of Q corresponding to the resonant eigenvalue. Near the resonant energy E = 1.806 eV, the channels which participate most in the resonance dynamics are clearly v=0 of the H_2 reactants and v'=2 of the HF products.

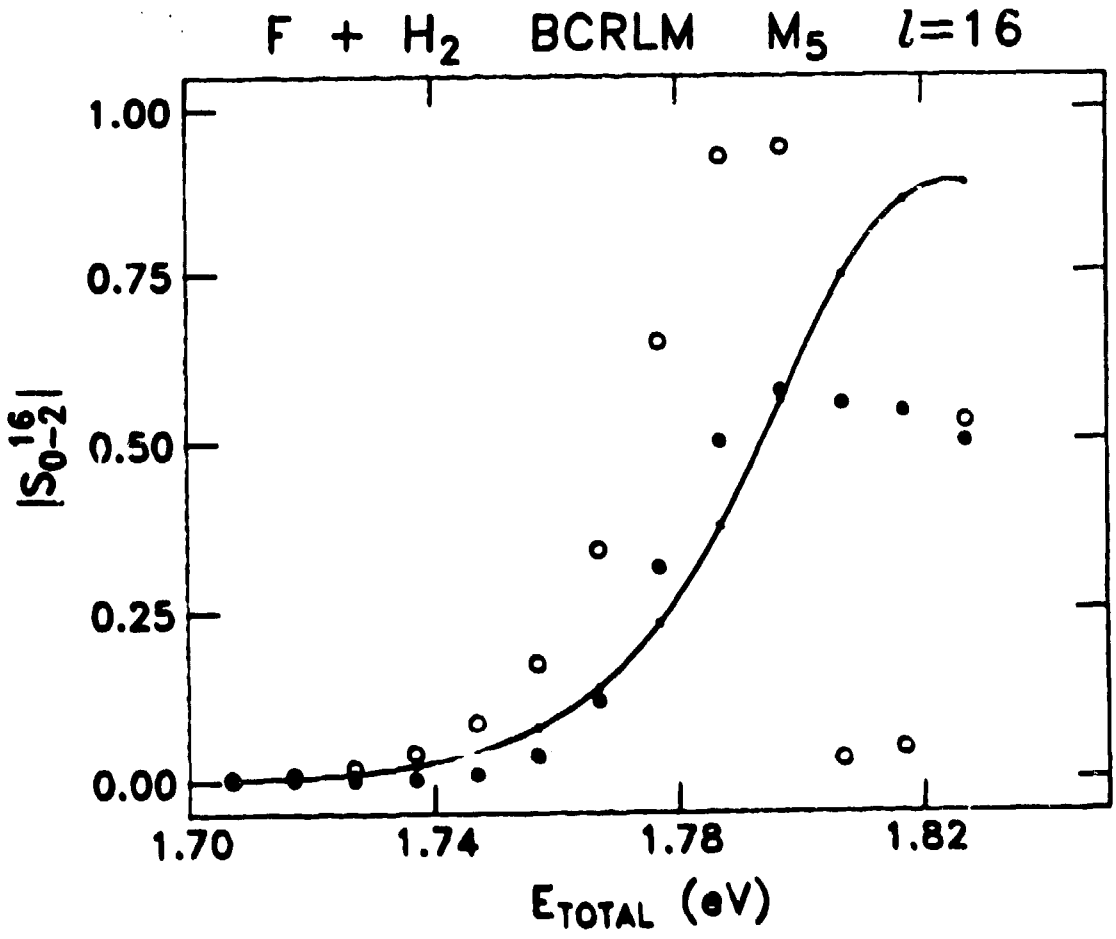

Figure 6. Magnitudes of background S-matrix elements for the reaction $F+H_2(v=0) \rightarrow HF(v'=2)+H$, partial wave $J=16$. The solid curve shows the full S-matrix elements, and the open and filled circles show two choices of background elements corresponding to the two phase choices for the partial widths (see text). The open circles are elements corresponding to a nonphysical root, the closed circles correspond to the physical root.

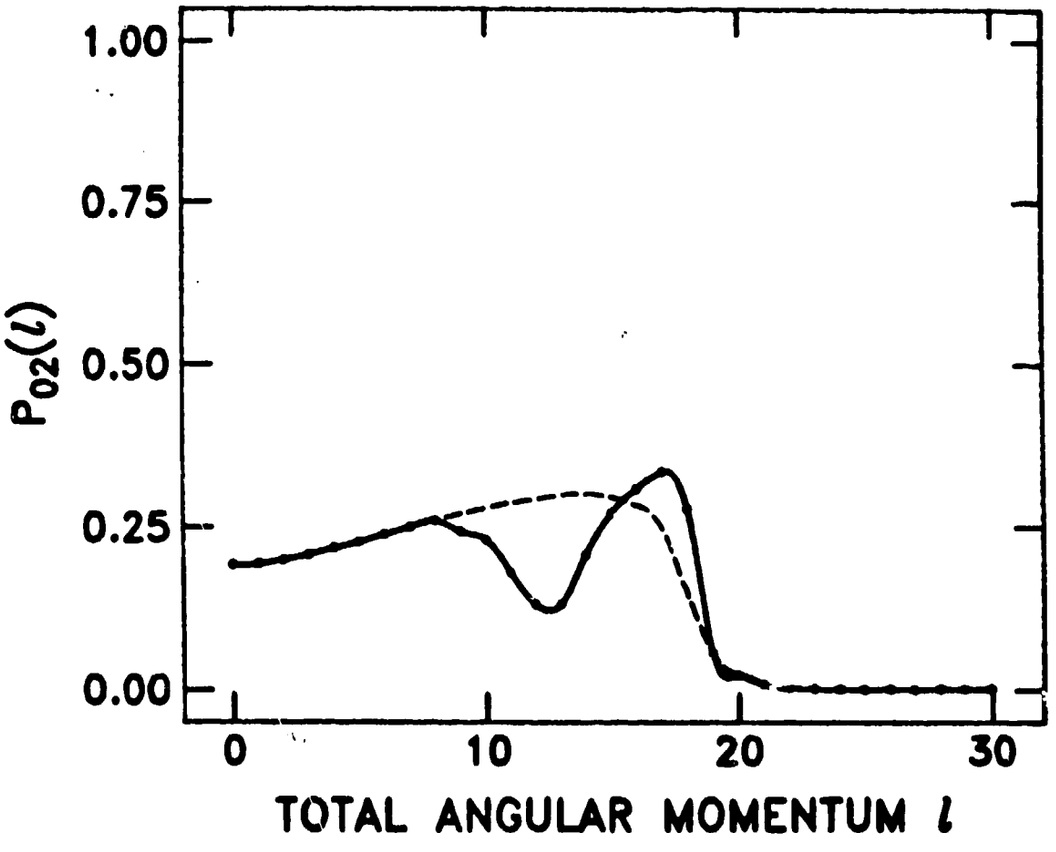

Figure 7. Background opacity function for the reaction $F+H_2(v=0) \rightarrow HF(v'=2)+H$ at E = 1.807 eV. The solid curve is the direct result of the extraction procedure discussed in the text, and the dashed curve is a smoothed version.

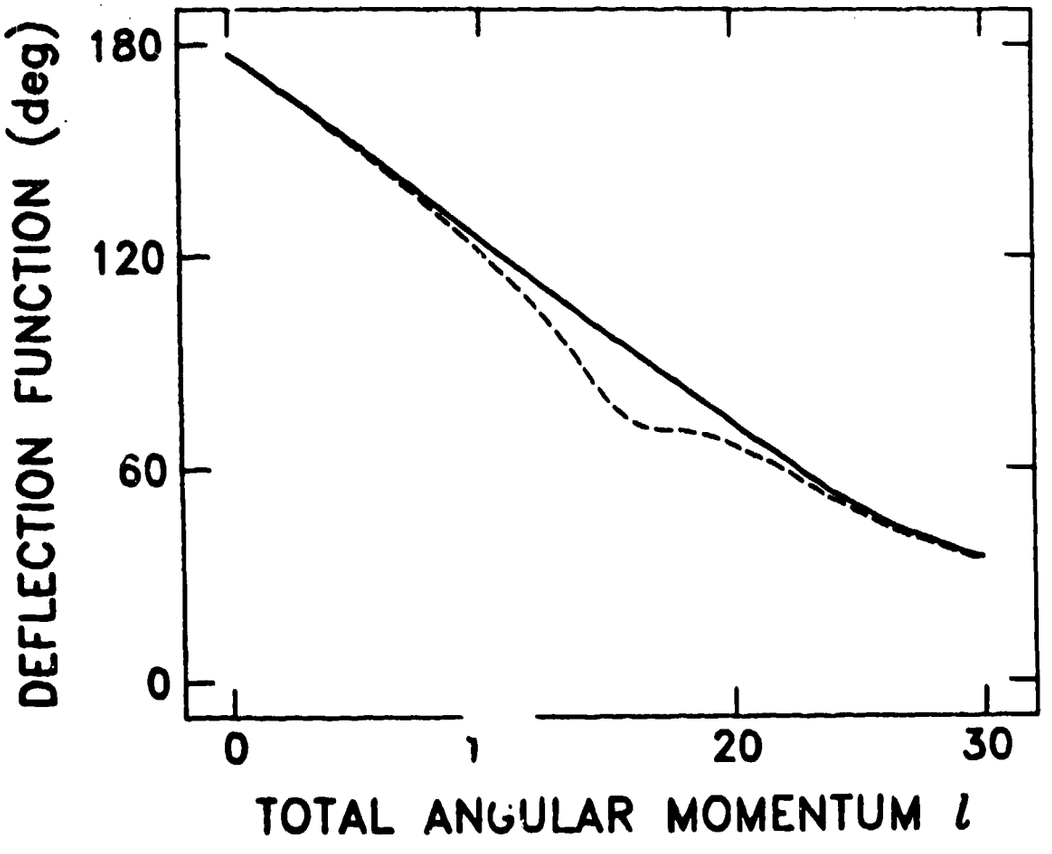

Figure 8. Background deflection function for the reaction $F+H_2$ → $HF(v'=2)+H$ at E = 1.807 eV. The solid curve removes the resonance contribution using Equation (23). The dashed curve reproduces the full deflection function of Figure 2 for comparison.

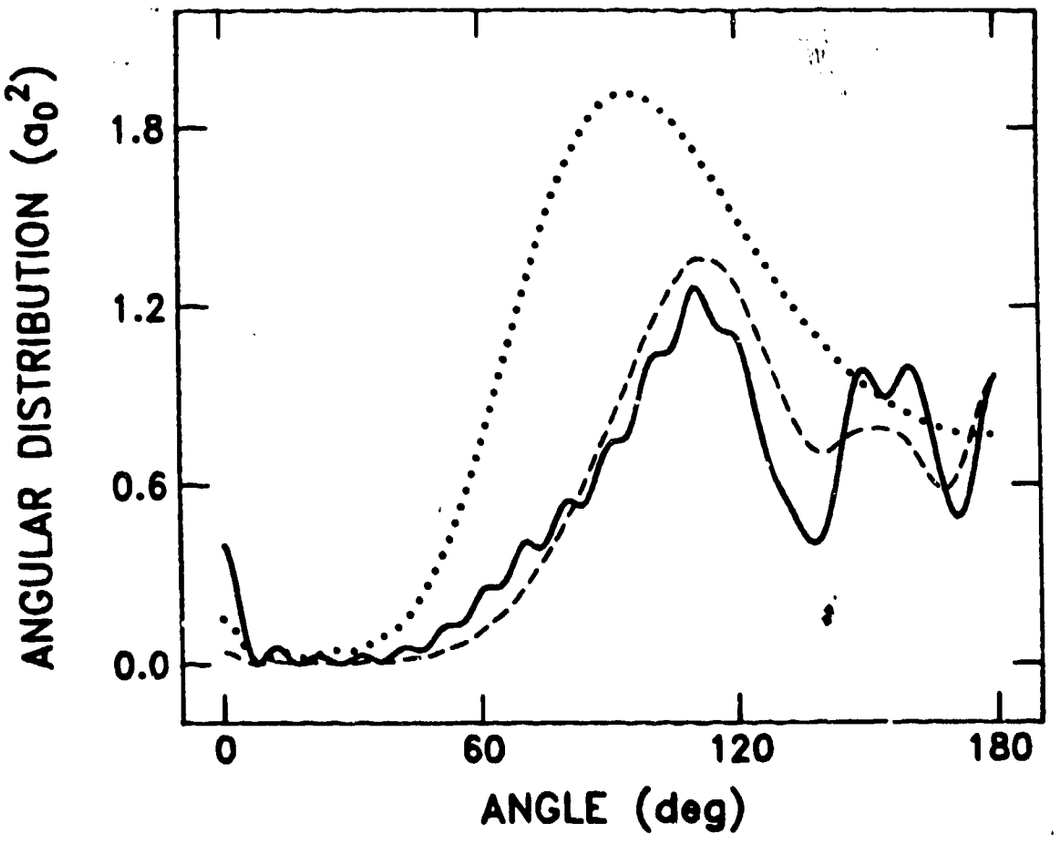

Figure 9. Background angular distributions for the reaction $F+H_2(v=0) \rightarrow HF(v'=2)+H$ at E = 1.807 eV. The solid curve used the opacity function shown in Figure 7 as a solid curve, and the smoother, dashed curve shows the angular distribution which results from the smoothed opacity function of Figure 7. The dotted curve reproduces the full angular distribution of Figure 3 for comparison.

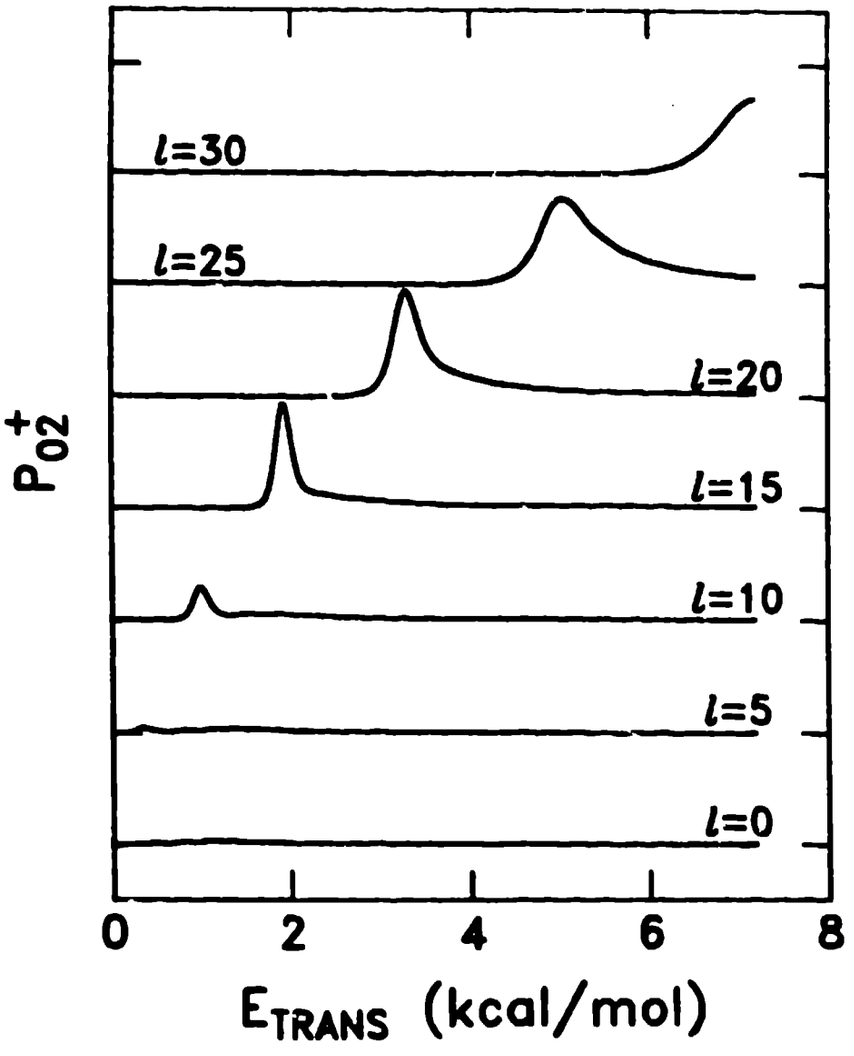

Figure 10. Reaction probabilities vs. energy for the reaction $F+H_2(v=0) \rightarrow HF(v'=2)+H$ on a recent modification (49) of the M5 surface. Curves are shown for partial waves $\ell=0,5,10,\ldots30$. Note the resonance feature which builds in at large partial waves.

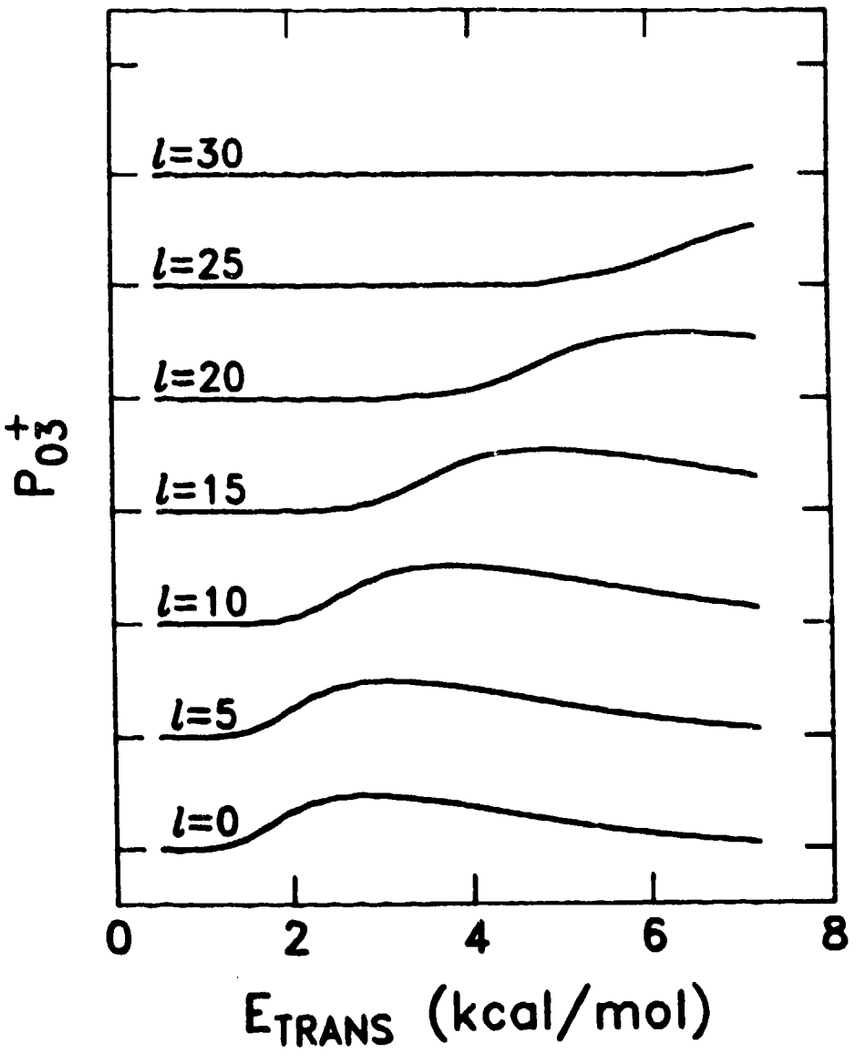

Figure 11. Reaction probabilities vs. energy for the reaction $F+H_2(v=0) \rightarrow HF(v'=3)+H$ on a recent modification (49) of the M5 surface. Curves are shown for $\ell=0,5,10,\ldots30$. Note the reduced delay in the threshold for reaction at low partial waves.

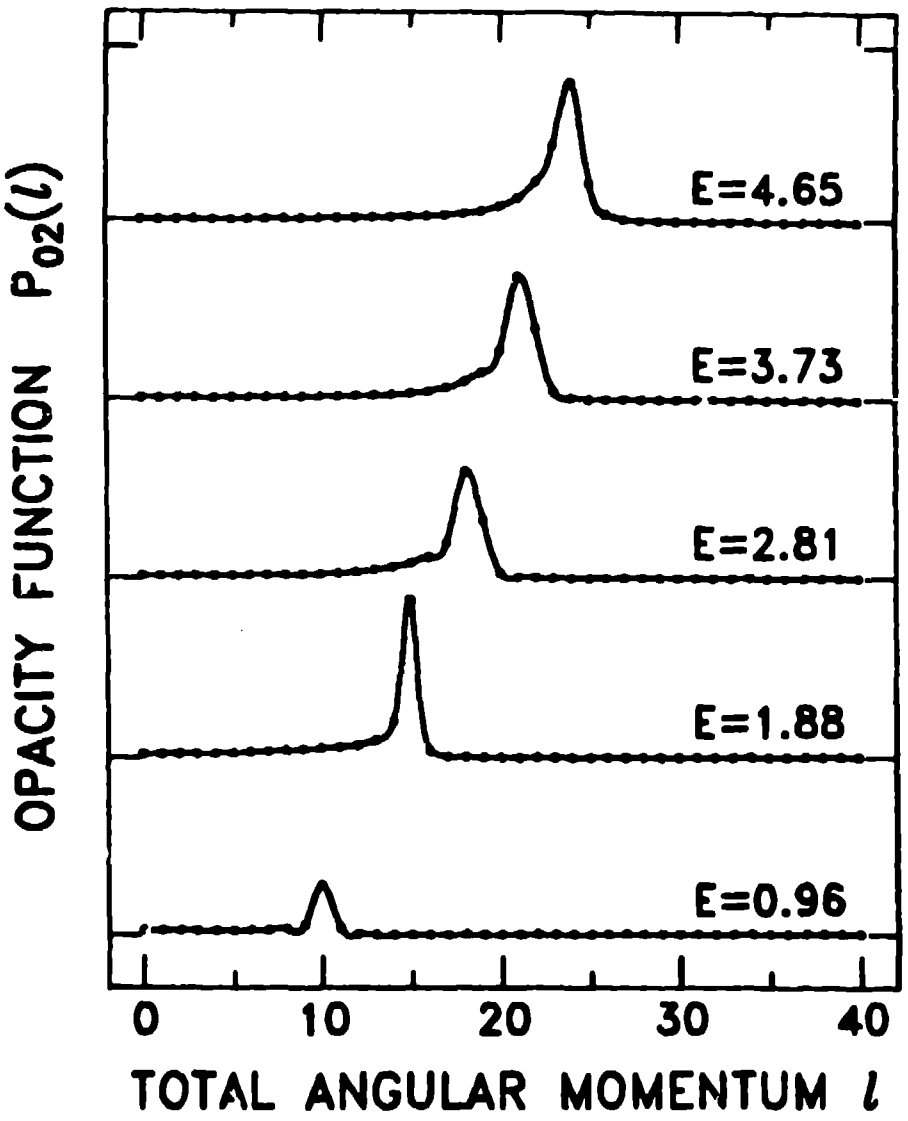

Figure 12. Opacity functions for the reaction $F+H_2(v=0) \rightarrow HF(v'=2)+H$ on a recent modification (49) of the M5 surface. Curves are shown at several scattering energies. Note that almost all the scattering at each energy arises from only a few, large l partial waves.

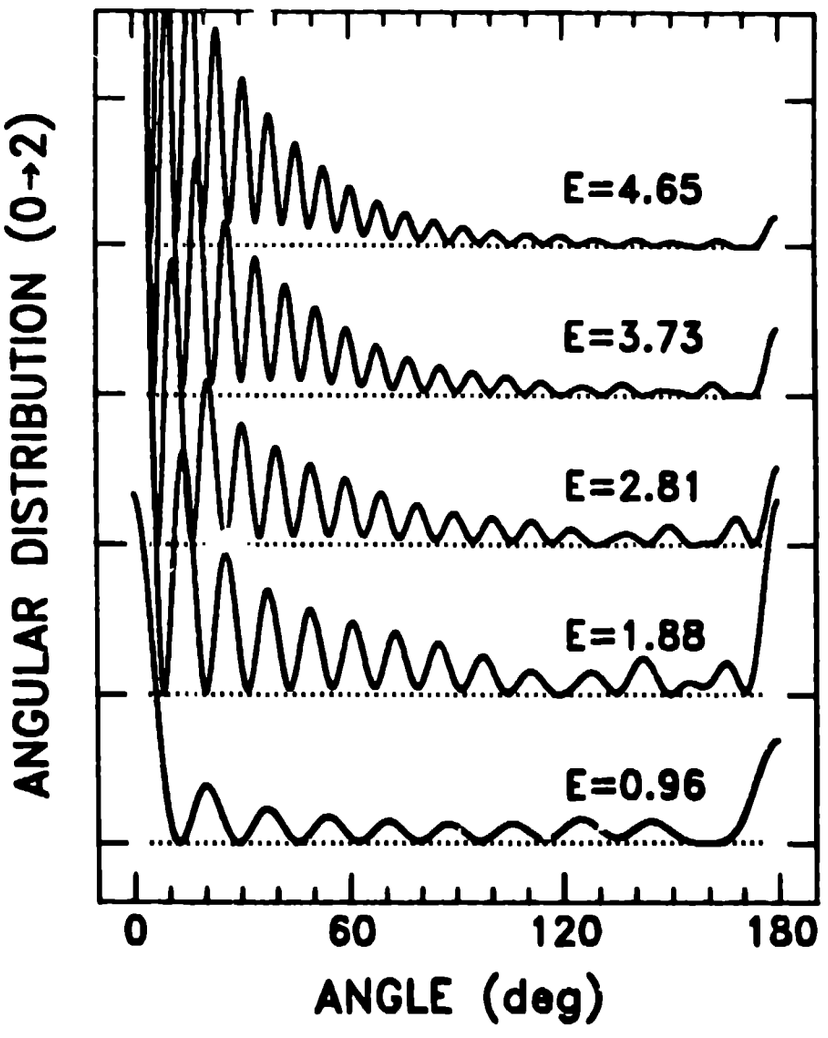

Figure 13. Angular distributions for the reaction $F+H_2(v=0) \rightarrow HF(v'=2)+H$ on a recent modification (49) of the MS surface. Curves are shown at the same energies as Figure 12.

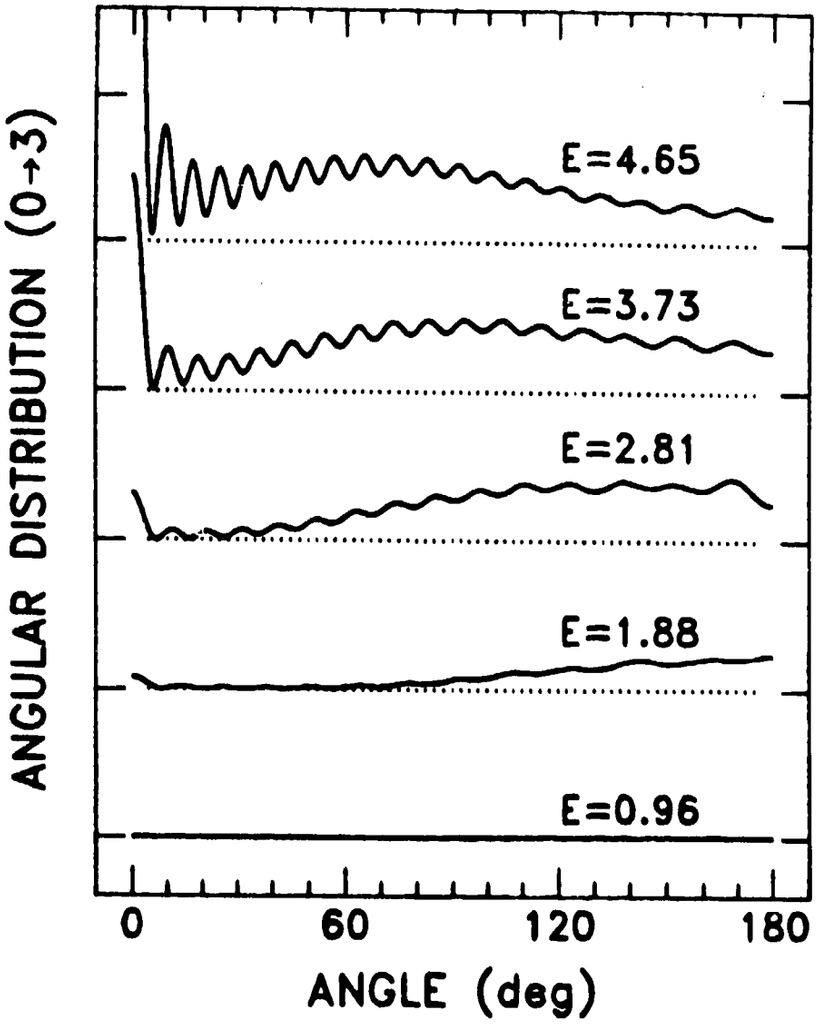

Figure 14. As in Figure 13, angular distribution for the reaction $F+H_2(v=0) \rightarrow HF(v'=3)+H$ on a recent modification of the M5 surface. The interference oscillations indicate that the HF(v'=3) channel participates in the resonance dynamics for this surface.

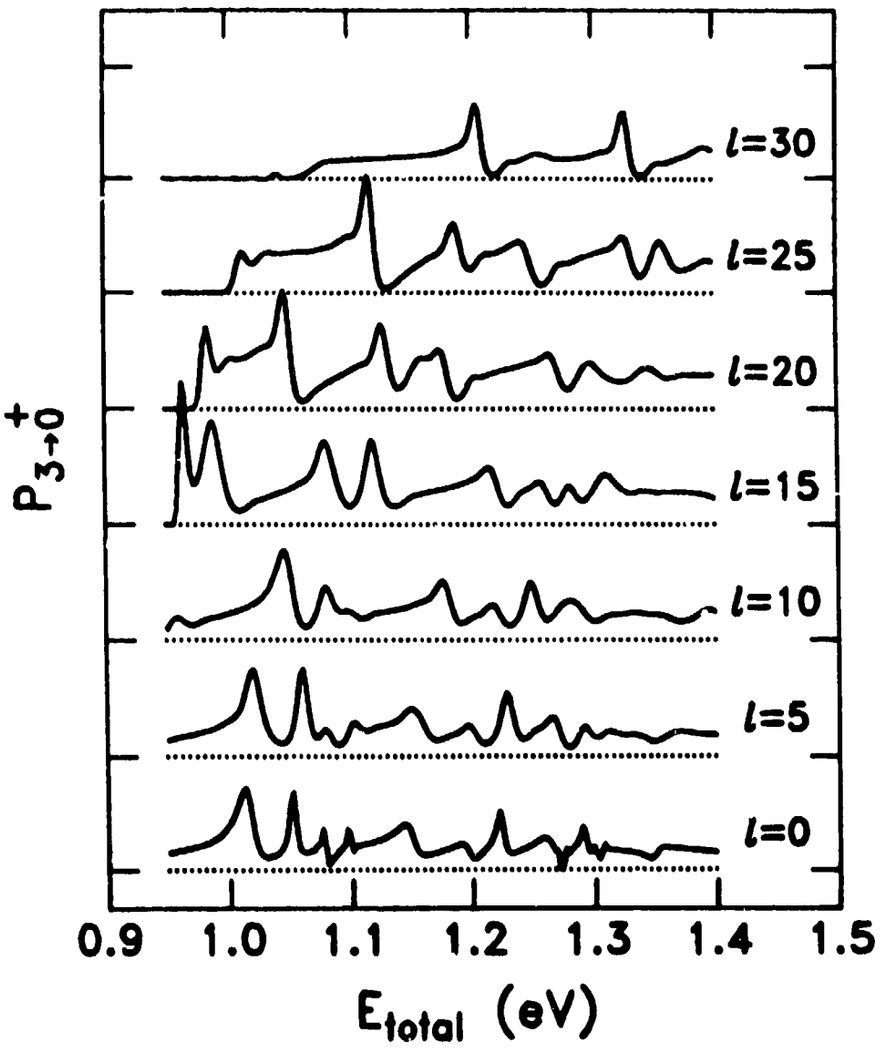

Figure 15. Reaction probabilities vs. energy for the reaction He + $H_2^+(v=3)$ → $HeH^+(v'=0)$+H on the DIM surface of reference (50). Curves are shown for ℓ=0,5,10,...,30.

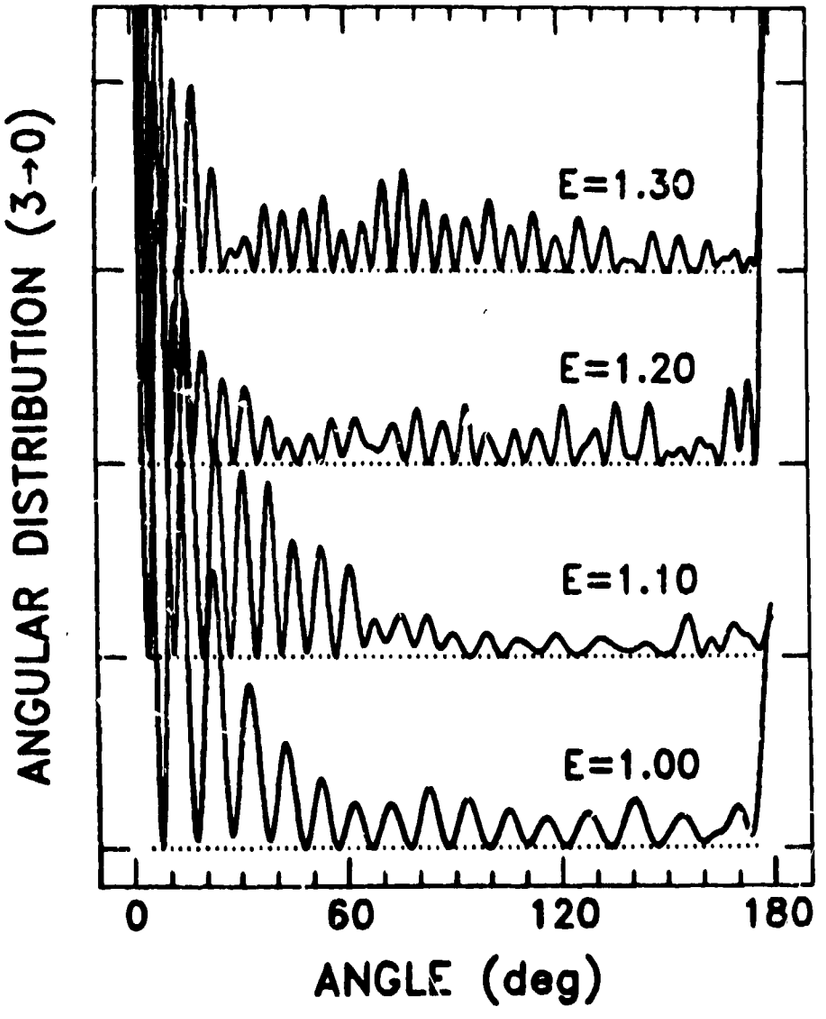

Figure 16. Angular distributions for the reaction $He + H_2^+(v=3) \rightarrow HeH^+(v'=0)+H$. Curves are shown at total energies (measured from the minimum of the H_2^+ entrance valley well) E = 1.0, 1.1, 1.2, and 1.3 eV.